The Astrophysical Journal Letters, 859:L24 (6pp), 2018 June 1 https://doi.org/10.3847/2041-8213/aac722

The *R*-Process Alliance: 2MASS J09544277+5246414, the Most Actinide-enhanced *R*-II Star Known

Erika M. Holmbeck[1,2], Timothy C. Beers[1,2], Ian U. Roederer[2,3], Vinicius M. Placco[1,2], Terese T. Hansen[4], Charli M. Sakari[5], Christopher Sneden[6], Chao Liu[7], Young Sun Lee[8], John J. Cowan[9], and Anna Frebel[2,10]
[1] Department of Physics, University of Notre Dame, Notre Dame, IN 46556, USA; eholmbec@nd.edu
[2] JINA Center for the Evolution of the Elements, USA
[3] Department of Astronomy, University of Michigan, 1085 South University Avenue, Ann Arbor, MI 48109, USA
[4] The Observatories of the Carnegie Institution of Washington, Pasadena, CA 91101, USA
[5] Department of Astronomy, University of Washington, Seattle, WA 98195, USA
[6] Department of Astronomy and McDonald Observatory, The University of Texas, Austin, TX 78712, USA
[7] Key Lab of Optical Astronomy, National Astronomical Observatories, CAS, 100012, Beijing, People's Republic of China
[8] Department of Astronomy and Space Science, Chungnam National University, Daejeon 34134, Republic of Korea
[9] HLD Department of Physics & Astronomy, University of Oklahoma, Norman, OK 73019, USA
[10] Department of Physics and Kavli Institute for Astrophysics and Space Research, Massachusetts Institute of Technology, Cambridge, MA 02139, USA
Received 2018 April 23; revised 2018 May 14; accepted 2018 May 14; published 2018 June 1

Abstract

We report the discovery of a new actinide-boost star, 2MASS J09544277+5246414, originally identified as a very bright ($V = 10.1$), extremely metal-poor ([Fe/H] $= -2.99$) K giant in the LAMOST survey, and found to be highly *r*-process-enhanced (*r*-II; [Eu/Fe] $= +1.28$]), during the snapshot phase of the *R*-Process Alliance (RPA). Based on a high signal-to-noise ratio (S/N), high-resolution spectrum obtained with the Harlan J. Smith 2.7 m telescope, this star is the first confirmed actinide-boost star found by RPA efforts. With an enhancement of [Th/Eu] $= +0.37$, 2MASS J09544277+5246414 is also the most actinide-enhanced *r*-II star yet discovered, and only the sixth metal-poor star with a measured uranium abundance ([U/Fe] $= +1.40$). Using the Th/U chronometer, we estimate an age of 13.0 ± 4.7 Gyr for this star. The unambiguous actinide-boost signature of this extremely metal-poor star, combined with additional *r*-process-enhanced and actinide-boost stars identified by the RPA, will provide strong constraints on the nature and origin of the *r*-process at early times.

Key words: Galaxy: halo – stars: abundances – stars: atmospheres – stars: individual (2MASS J09544277+5246414) – stars: Population II

Supporting material: tar.gz file

1. Introduction

First described by Burbidge et al. (1957) and Cameron (1957), the rapid neutron-capture ("*r*-") process is the physical mechanism responsible for synthesizing roughly half of the elements heavier than iron present in the solar system. The astrophysical site of the *r*-process is currently a topic of curiosity and debate, but recent follow-up observations on the gravitational wave event GW170817 (Abbott et al. 2017) strongly support the merging of two neutron stars in a binary system as one possible production site. Photometric (Drout et al. 2017) and spectroscopic (Shappee et al. 2017) evidence for the presence of unstable lanthanide isotopes produced by the *r*-process have been identified from observations of the kilonova source SSS17a associated with the neutron star merger (Cowperthwaite et al. 2017; Kilpatrick et al. 2017). Events such as magneto-rotational instability ("jet") supernovae also remain a viable astrophysical site for the "main" *r*-process (see, e.g., Nishimura et al. 2017).

Individual *r*-process-enhanced stars in the halo of the Milky Way have recorded in their photospheres the nucleosynthetic products of *r*-process events that occurred early in Galactic history. These stars are characterized by their typically low metallicities ([Fe/H] $\lesssim -2$) and moderate to large over-abundances of *r*-process elements. We use the designations "*r*-I": $+0.3 \leqslant$ [Eu/Fe] $\leqslant +1.0$ and "*r*-II": [Eu/Fe] $> +1.0$ to quantify the observed level of *r*-process enhancement (Beers & Christlieb 2005). The *r*-process elements present in the photospheres of *r*-process-enriched stars likely reflect the contributions from one to at most a few *r*-process events preceding their formation.

About 40 *r*-II stars are currently known in the Galactic halo; 10 of these were recently identified through an ongoing search for *r*-process-enhanced stars, conducted as part of the *R*-Process Alliance (RPA; Hansen et al. 2018; Sakari et al. 2018). Another seven *r*-II stars have been identified in the ultra faint dwarf (UFD) galaxy Reticulum II (Ji et al. 2016; Roederer et al. 2016). The main *r*-process elemental-abundance pattern (Ba to Hf) of *r*-I and *r*-II stars is strikingly homogeneous and closely follows the *r*-process pattern observed in the solar system for stars covering a wide range of metallicities (Sneden 2002; Siqueira Mello et al. 2014; Hansen et al. 2017). The universality of the main *r*-process pattern among Milky Way halo stars, UFDs, and classical dwarf galaxies suggests that either the *r*-process behaves uniformly regardless of its astrophysical site, or that the observed *r*-process material comes from one type of *r*-process-element production event.

The identification and analysis of metal-poor, *r*-process-enhanced stars is essential for elucidating the nature and origin of the astrophysical *r*-process. Although the elemental-abundance patterns of *r*-process-enriched stars are relatively homogeneous among the lanthanides, the actinide abundances vary significantly; about 30% of *r*-process-enhanced stars exhibit Th/Eu abundance ratios a factor of 2–3 higher than the majority of other *r*-process-enriched stars (see Hill et al. 2002;

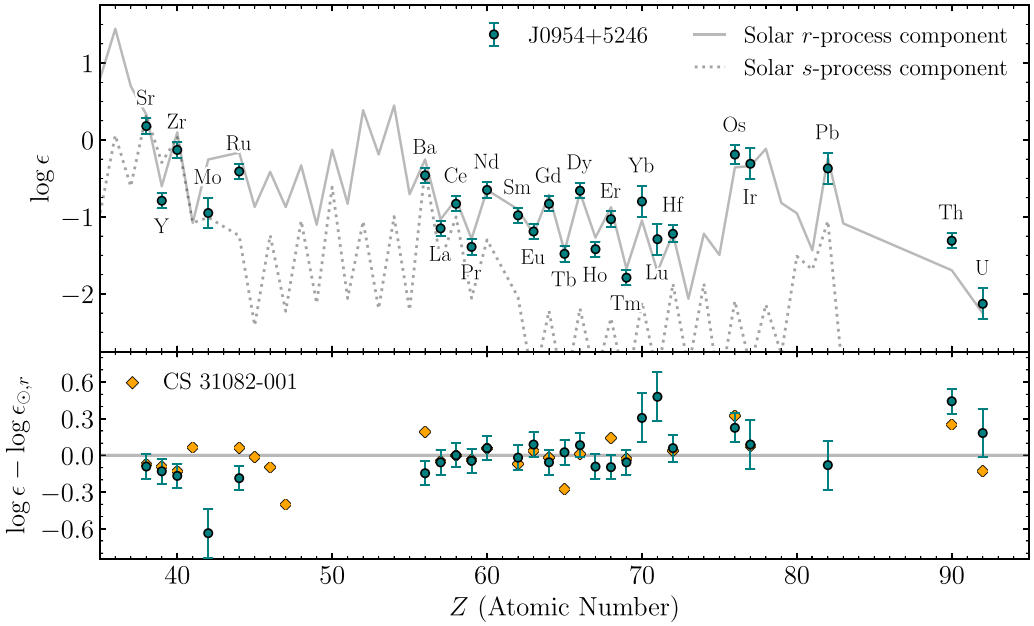

Figure 1. Top panel: full *r*-process elemental-abundance pattern of J0954+5246. Also shown are the scaled-Solar *s*-process abundances (dotted line). The Solar *r*-process component (solid line) is the abundance residual from the *s*-process. Both components are normalized to Sr. Solar abundances are from Asplund et al. (2009); *s*-process abundance fractions are from Arlandini et al. (1999). Bottom panel: difference between the observed abundances and the Solar *r*-process component for J0954+5246 and observations of the canonical actinide-boost star CS 31082–001, as reported by Hill et al. (2002). The residuals in the bottom panel are normalized to the average residual between Ba and Tm.

Table 1
Derived Parameters for J0954+5246

Parameter	LAMOST	SSPP	TS-23[a]
$T_{\rm eff}$ (K)	4462 ± 110	4340 ± 150	4340 ± 125
log *g* (cgs)	0.91 ± 0.19	0.6 ± 0.30	0.41 ± 0.20
[Fe/H]	−2.46 ± 0.11	−3.16 ± 0.15	−2.99 ± 0.10
ξ (km s^{-1})	···	···	2.28 ± 0.20
[C/Fe]	···	−0.34	−0.50 ± 0.20
MJD	57030	57030	58128
RV (km s^{-1})	−71 ± 5	−71.9 ± 1.8	−67.7 ± 0.1

Note.
[a] Final parameters adopted for this work.

Mashonkina et al. 2014). The mechanism for producing this "actinide boost" is neither well-studied nor well-understood and suffers from low number statistics. Studying actinide-boost stars can provide clues to the different astrophysical conditions necessary to produce elements beyond the third *r*-process peak and help to distinguish between suggested astrophysical sites for the *r*-process.

In this Letter we present the elemental-abundance analysis, based on the high-resolution spectroscopic follow-up conducted as part of the RPA, of a newly identified actinide-boost *r*-II star: 2MASS J09544277+5246414 (hereafter J0954 +5246). Not only is J0954+5246 the sixth metal-poor star with a uranium measurement, it is also the brightest ($V = 10.095$; APASS; Henden et al. 2016) and the most actinide-enhanced ([Th/Eu] = +0.37) *r*-II star currently known. Due to its brightness, extremely low metallicity, and lack of carbon enhancement, we are able to report measurements for 42 elements available from ground-based, optical observations.

2. Observations and Analysis

J0954+5246 was first identified as a candidate very metal-poor K giant in the LAMOST (DR4) Survey (Liu et al. 2014). The SEGUE Stellar Parameter Pipeline (SSPP; Lee et al. 2008a, 2008b) was used to estimate the atmospheric parameters ($T_{\rm eff}$, log *g*, and [Fe/H])—as well as its carbon-to-iron ratio ([C/Fe], as described in Lee et al. 2013)—from the LAMOST medium-resolution data. The metallicity and [C/Fe] estimated by the SSPP revealed J0954+5246 to be extremely metal-poor, non-carbon-enhanced, and with a low effective temperature, suitable for inclusion in the RPA search for *r*-process-enhanced stars.

We carried out high-resolution ("portrait") spectroscopic observations during 2018 using the Harlan J. Smith 107-in (2.7 m) telescope and the TS23 echelle spectrograph (Tull et al. 1995) at McDonald Observatory. The high-resolution setup uses a 1.″2 slit and 1 × 1 binning, yielding a resolving power of $R \sim 60{,}000$, with full wavelength coverage of 3600–5800 Å and partial wavelength coverage up to 10,000 Å. From the co-addition of nine spectra (total exposure time 15,600 s), a final signal-to-noise ratio (S/N) of 90 per resolution element at 4100 Å was achieved. The data were reduced using standard IRAF packages (Tody 1993).

Equivalent widths (EWs) of 125 Fe I and 27 Fe II lines were measured using the `splot` task in IRAF, fitting a Gaussian profile to each line, and deblending where necessary. Individual Fe I and Fe II abundances were derived from their EWs using the current version of the LTE stellar line analysis code `MOOG`[11] (Sneden 1973), which includes an appropriate treatment of scattering (Sobeck et al. 2011). We use α-enhanced ([α/Fe] = 0.4) ATLAS9 model atmospheres (Castelli & Kurucz 2004). A list of all Fe lines used to determine the atmospheric parameters of J0954+5246 is provided in a .tar.gz package.

[11] https://github.com/alexji/moog17scat

Table 2
Derived Elemental Abundances of J0954+5246

Species	$\log \epsilon_{\odot}$	$\log \epsilon$	[X/H]	[X/Fe]	$\sigma_{\log \epsilon}$	N
C (CH)	8.43	4.94	−3.49	−0.50[a]	0.20	1
Na I	6.24	3.53	−2.72	0.28	0.10	2
Mg I	7.60	5.25	−2.35	0.64	0.10	4
Al I	6.45	3.06	−3.39	−0.40	0.20	1
Ca I	6.34	3.60	−2.74	0.25	0.10	14
Sc II	3.15	−0.02	−3.17	−0.18	0.10	7
Ti I	4.95	1.97	−2.98	0.01	0.10	9
Ti II	4.95	2.17	−2.78	0.21	0.10	11
V II	3.93	0.94	−2.99	0.00	0.10	2
Cr I	5.64	2.34	−3.30	−0.31	0.10	7
Cr II	5.64	2.81	−2.84	0.16	0.10	2
Mn I	5.43	1.64	−3.79	−0.80	0.14	3
Fe I	7.50	4.51	−2.99	0.00	0.12	27
Fe II	7.50	4.51	−2.99	0.00	0.12	125
Co I	4.99	1.98	−3.02	−0.02	0.10	2
Ni I	6.22	3.26	−2.96	0.03	0.10	3
Cu I	4.19	<0.15	<−4.04	<−1.05		1
Zn I	4.56	1.72	−2.84	0.15	0.20	1
Ga I	3.04	<0.05	<−2.99	<0.00		1
Sr I	2.87	0.88	−1.99	1.00	0.20	1
Sr II	2.87	0.18	−2.69	0.30	0.10	3
Y II	2.21	−0.79	−3.00	−0.01	0.10	12
Zr II	2.58	−0.13	−2.71	0.28	0.10	4
Mo I	1.88	−0.95	−2.83	0.16	0.20	1
Ru I	1.75	−0.41	−2.16	0.84	0.10	2
Ba II	2.18	−0.46	−2.64	0.35	0.10	3
La II	1.10	−1.15	−2.25	0.74	0.10	16
Ce II	1.58	−0.83	−2.41	0.58	0.10	13
Pr II	0.72	−1.39	−2.11	0.88	0.10	7
Nd II	1.42	−0.65	−2.07	0.92	0.10	14
Sm II	0.96	−0.98	−1.94	1.05	0.10	11
Eu II	0.52	−1.19	−1.71	1.28	0.10	4
Gd II	1.07	−0.83	−1.90	1.09	0.10	7
Tb II	0.30	−1.48	−1.78	1.21	0.10	4
Dy II	1.10	−0.66	−1.76	1.23	0.10	6
Ho II	0.48	−1.42	−1.90	1.10	0.10	4
Er II	0.92	−1.03	−1.95	1.04	0.10	4
Tm II	0.10	−1.79	−1.89	1.10	0.10	4
Yb II	0.84	−0.80	−1.64	1.35	0.20	1
Lu II	0.10	−1.29	−1.39	1.60	0.20	1
Hf II	0.85	−1.22	−2.07	0.92	0.11	2
Os I	1.40	−0.19	−1.59	1.40	0.12	3
Ir I	1.38	−0.31	−1.69	1.30	0.20	1
Pb I	1.75	−0.37	−2.12	0.87	0.20	1
Th II	0.02	−1.31	−1.36	1.63	0.10	3
U II	−0.54	−2.13	−1.59	1.40	0.20	1

Note.
[a] Natal [C/Fe] = +0.24, based on corrections from Placco et al. (2014).

All other elemental abundances were derived from the spectral synthesis of features in the portrait spectrum using MOOG. Oscillator strengths and excitation potentials for all lines in this work were generated with `linemake`,[12] which compiles recent, accurate atomic transition data and includes hyperfine splitting. Isotopic ratios, employed when synthesizing features with hyperfine splitting and isotopic shift effects, were taken from the Solar *r*-process ratios in Sneden et al. (2008).

[12] https://github.com/vmplacco/linemake

J0954+5246 is a cool, extremely metal-poor giant; at such extremes, it becomes difficult to determine atmospheric parameters based on spectroscopy alone. Over a large range of excitation potentials, the spectroscopically derived Fe I abundances equilibrate at 4100 K. However, Fe I and Fe II abundance equilibration fails at these low effective temperatures, disagreeing by about 0.3 dex. Instead of a pure spectroscopic approach, we first use the temperature scaling for giant stars from Alonso et al. (1999), applied to 2MASS photometry (Skrutskie et al. 2006), to obtain a $T_{\rm eff}$ estimate of 4340 K, based on the $(J-K)$ color of 0.716.[13] After applying the correction from Frebel et al. (2013) to the 4100 K found previously, we find a spectroscopic temperature of 4360 K, which agrees with the photometric estimate and validates the spectroscopic method, despite the differences that arise between Fe I and Fe II abundances at low temperatures. The reddening is sufficiently low ($E(B-V)=0.007$; Schlafly & Finkbeiner 2011) that it does not significantly affect the $(J-K)$ color. After fixing the temperature to the photometric estimate of 4340 K, ionization equilibration was carried out to find the surface gravity and metallicity. Microturbulence was determined by minimizing the Fe I and Fe II abundance trends in reduced EW. Carbon abundance was measured based on high-resolution spectral synthesis of the 4300 Å CH *G*-band. Table 1 summarizes the derived atmospheric parameters (and their estimated errors) for this star from the medium- and high-resolution spectra. Measured radial velocities are also reported in Table 1; based on the similarity between radial velocity measurements, there is no indication of binarity for J0954+5246.

3. The *r*-process Pattern

Derived neutron-capture-element abundances of J0954+5246 are shown in Figure 1. The abundances unequivocally match a scaled-Solar pure *r*-process pattern, with no apparent contribution from the *s*-process. Also shown in Figure 1 is a comparison to the elemental-abundance pattern of the canonical actinide-boost star, CS 31082–001 (Hill et al. 2002). Table 2 lists the derived abundances for all elements identified in J0954+5246, their comparison to Asplund et al. (2009) Solar abundances, the uncertainty of the abundance, and the number of lines measured. A complete linelist of all measured transitions and derived individual abundances is provided in the .tar.gz package. We adopt a minimum uncertainty of 0.10 dex. For elements with only one feature, a 0.2 dex uncertainty is assumed. Important spectral features, including Sr, Ba, and Eu—used to classify *r*-process-enhancement in metal-poor stars—are shown in Figure 2. Abundances of the elements from C to Ga in J0954+5246 resemble those of normal metal-poor halo stars. In the following, we focus on the neutron-capture element abundances.

As with all *r*-II stars, the heavy-element abundance pattern of J0954+5246 reproduces the observed scaled-Solar lanthanide abundances, with deviations greater than the formal uncertainties for only a few elements. However, the most striking difference between J0954+5246 and other *r*-II stars is its actinide signature.

[13] This photometric temperature matches that obtained from the SSPP, based on the medium-resolution spectrum.

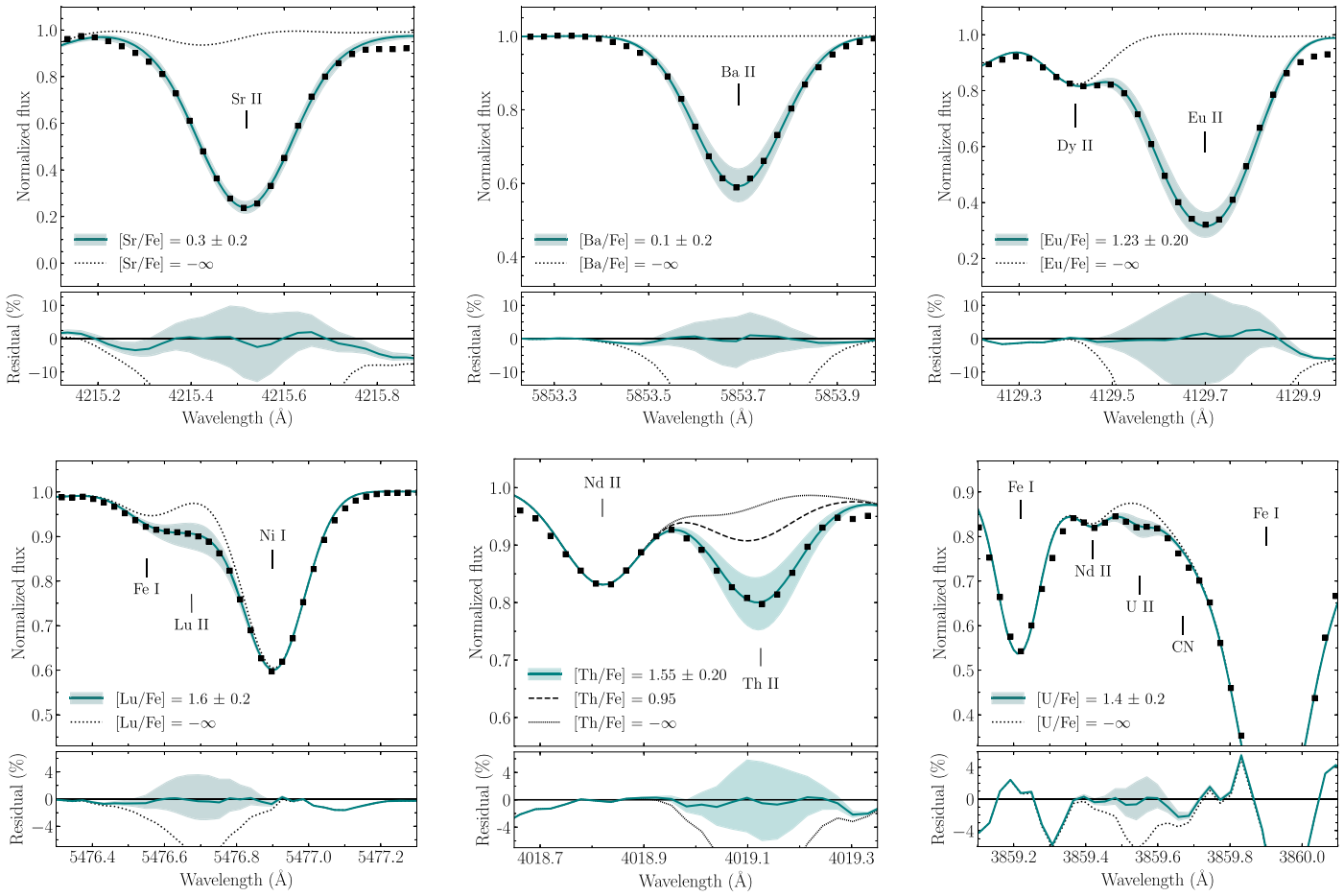

Figure 2. Relevant syntheses and derived abundances for important *r*-process elements present in J0954+5246. The top panels of each plot show the best-fit syntheses (solid lines) and 0.2 dex uncertainties (shaded regions) compared to the observed spectrum (points). Key features are labeled. The bottom panels show the residuals between the observed spectrum and the synthetic fits. Derived abundances corresponding to the plotted syntheses are indicated in each legend. The [Th/Fe] = 0.95 synthesis corresponds to a typical non-actinide-enhanced Th II line profile.

3.1. Light Neutron-capture Elements

The elements Sr, Y, Zr, Mo, and Ru were measured in this star; atomic transitions of Rh, Pd, and Ag occur at wavelengths bluer than the instrumental system limit for efficient throughput, preventing measurement of their abundances. It has been previously noted that a significant spread in the light neutron-capture elements exists in *r*-process-enhanced stars, with *r*-I stars generally exhibiting stronger relative first-peak enhancement (Siqueira Mello et al. 2014). This spread is often attributed to a separate *r*-process, which is referred to as a limited, or weak, *r*-process (Wanajo & Ishimaru 2006; Hansen et al. 2012; Frebel 2018), and is distinct from that responsible for the production of second- and third-peak elements. Compared to the scaled-Solar pattern, the light *r*-process elements in J0954+5246 are indeed slightly lower, indicating little limited-*r* contribution. It should be noted that Mo has a significant *p*-process component, which is not accounted for in the Solar *r*-process residual, likely causing its apparent under-abundance (Meyer 1994).

3.2. Heavy Neutron-capture Elements

We were able to derive abundances for all stable elements between Ba and Hf, as well as Os, Ir, and Pb. Like most *r*-II stars, the abundance pattern of J0954+5246 in this region agrees well with scaled-Solar *r*-process values, with some deviations. Intriguingly, the abundance of Yb II is much higher than the scaled-Solar *r*-process value in J0954+5246; this overabundance is also observed in CS 29497–004 (Hill et al. 2017) and CS 22892–052 (Sneden et al. 2008), neither of which display an actinide boost. However, it should be noted that the Yb abundance is derived from only one feature, and is affected by hyperfine splitting, which is included in this synthesis. Similarly, Lu and Ir appear over-abundant relative to the Solar *r*-process pattern, but these elements each have just one optical feature suitable for abundance derivations. Figure 2 shows the synthesis of the lutetium feature from which we derived the Lu II abundance.

3.3. Thorium, Uranium, and the Actinide Boost

Uranium is among the most difficult elements to measure in a star. However, being able to measure uranium—together with thorium—provides clues to the nature and possible site of the *r*-process that synthesized the actinides. Three lines of Th II were measured in this star, spanning an abundance range of 0.23 dex. Only one line of U II was measured; syntheses are shown in Figure 2. The actinide-to-lanthanide ratio of [Th/Eu] = +0.37 demonstrates the actinide-boost designation of J0954+5246.

Figure 3 shows the log ϵ (Th/Eu) abundances of halo *r*-I and *r*-II stars; non-actinide-boost stars typically have log ϵ (Th/Eu) values near −0.5. Even allowing for a 0.15 dex uncertainty, the log ϵ (Th/Eu) abundance of J0954+5246 is larger than its

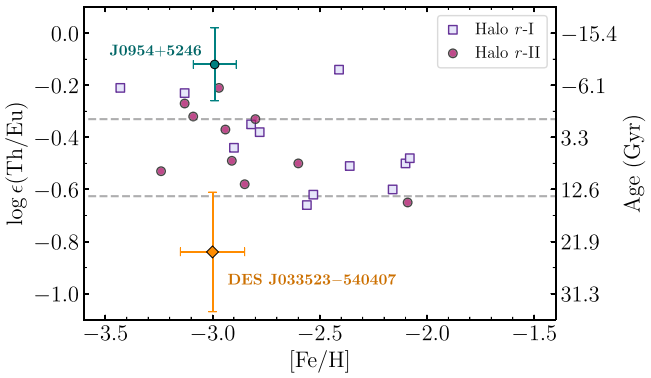

Figure 3. Th/Eu abundances vs. metallicity for known *r*-I and *r*-II stars where a Th measurement is provided. Also shown is the Reticulum II member, DES J033523−540407, reported by Ji & Frebel (2018). The right axis shows the Th/Eu age calculated based on Schatz et al. (2002) production ratios. Horizontal lines indicate physical limits on the age (i.e., 0 and 13.8 Gyr). Data were generated using JINAbase (Abohalima & Frebel 2017), supplemented by measurements from Mashonkina et al. (2014), Roederer et al. (2014), Hill et al. (2017), Placco et al. (2017), and Sakari et al. (2018).

non-actinide-boost cousins by a factor of ∼2, making it the most actinide-enhanced *r*-II star currently known. The actinide enhancement of J0954+5246 is even larger than that of the canonical actinide-boost star CS 31082−001 ([Th/Eu] = +0.20; Hill et al. 2002).

4. Discussion and Conclusion

The scatter of the Sr–Y–Zr-group abundances among *r*-process-enhanced stars may be attributed to different levels of production by the limited *r*-process, and thus the production of the first *r*-process peak can be decoupled from the second and third peaks. However, it seems unlikely that the actinides can be similarly decoupled from the main *r*-process, or attributed to a separate *r*-process entirely. The presence of the actinide boost demonstrates that a real variation exists among the actinide abundances. Therefore, measuring Th (and U) abundances for a larger number of *r*-process-enhanced stars is essential to distinguish between possible astrophysical *r*-process sites and to determine what conditions enable strong actinide production. Specifically, actinide enhancement could indicate fission cycling in *r*-process nucleosynthesis, which may only occur under certain astrophysical conditions. We are currently exploring the effect of fission cycling in the low-entropy dynamical ejecta of a neutron star merger as one possibility for the origin of the actinide-boost phenomenon (E. M. Holmbeck et al. 2018, in preparation).

On the other hand, there may exist evidence for *weak* actinide production. Ji & Frebel (2018) measured thorium for the brightest *r*-II star in the UFD galaxy Reticulum II: DES J033523−540407. This star exhibits an *under*-abundance of thorium, relative to europium, even though the rest of the main *r*-process is consistent with and other *r*-process-enhanced stars. The $\log \epsilon$ (Th/Eu) abundance of DES J033523−540407 is shown relative to its Milky Way counterparts in Figure 3. Such a low thorium abundance has not yet been observed in Milky Way halo stars, which brings into question the type of *r*-process that could underproduce the actinides.

The presence of long-lived radioactive actinides allows an approximate age determination by radioactive decay dating, as described in Placco et al. (2017). In the absence of a uranium measurement, the Th/Eu chronometer is used to derive ages by comparing them to a set of initial production ratios from *r*-process simulations, e.g., from Schatz et al. (2002). However, in actinide-boost stars, using the Th/Eu ratio leads to unphysical values, as the measured Th/Eu ratio may be higher than the theoretical initial production ratio. To our knowledge, none of the existing *r*-process nucleosynthesis models can account for the abundance pattern observed in actinide-boost stars. Notwithstanding this shortcoming, the Th/U chronometer can still be used to estimate stellar ages because the actinide boost affects thorium and uranium proportionally. The Th/U chronometer is insensitive to the boost and thus leads to more realistic ages of actinide-boost stars than the Th/Eu chronometer.

Using the production ratios from Schatz et al. (2002), the Th/U age is 13.0 ± 4.7 Gyr, commensurate with its low metallicity. Uncertainties on the age contain only the measured abundance uncertainty and do not include those on the production ratios. The Th/Eu and U/Eu ages are −9.5 Gyr and 5.8 Gyr, respectively. These ages can be made to agree with the Th/U age of 13.0 Gyr by boosting the initial production ratios of thorium and uranium by a factor of 3.1. In a similar analysis, Schatz et al. (2002) found a "boost factor" of 2.5 for CS 31082–001.

Values for this boost factor vary, as Th/Eu abundances are not found at discrete enhancement levels, but rather, cover a range. With refined stellar main *r*-process abundances—particularly for Th, U, and the third *r*-process-peak elements, where few features exist from which to derive abundances—as well as species that can only be measured from UV data, we may find clues that are unique to and correlated with actinide production, and thereby characterize the actinide boost and better understand its origin.

E.M.H., T.C.B., I.U.R., and V.M.P. acknowledge partial support for this work from grant PHY 14-30152; Physics Frontier Center/JINA Center for the Evolution of the Elements (JINA-CEE), awarded by the US National Science Foundation. This work has been supported in part by NSF grant AST1616040 to C.S. Y.S.L. acknowledges support from the National Research Foundation of Korea grant funded by the Ministry of Science and ICT (No.2017R1A5A1070354, NRF-2015R1C1A1A02036658, and NRF-2018R1A2B6003961).

Facilities: Smith, LAMOST.

Software: `IRAF` (Tody 1993), `linemake` (https://github.com/vmplacco/linemake), `MOOG` (https://github.com/alexji/moog17scat; Sneden 1973; Sobeck et al. 2011), `Matplotlib` (Hunter 2007).

ORCID iDs

Erika M. Holmbeck https://orcid.org/0000-0002-5463-6800
Timothy C. Beers https://orcid.org/0000-0003-4573-6233
Ian U. Roederer https://orcid.org/0000-0001-5107-8930
Vinicius M. Placco https://orcid.org/0000-0003-4479-1265
Terese T. Hansen https://orcid.org/0000-0001-6154-8983
Charli M. Sakari https://orcid.org/0000-0002-5095-4000
Christopher Sneden https://orcid.org/0000-0002-3456-5929
Chao Liu https://orcid.org/0000-0002-1802-6917
Young Sun Lee https://orcid.org/0000-0001-5297-4518
Anna Frebel https://orcid.org/0000-0002-2139-7145

References

Abbott, B. P., Abbott, R., Abbott, T. D., et al. 2017, PhRvL, 119, 161101
Abohalima, A., & Frebel, A. 2017, arXiv:1711.04410
Alonso, A., Arribas, S., & Martínez-Roger, C. 1999, A&AS, 140, 261
Arlandini, C., Käppeler, F., Wisshak, K., et al. 1999, ApJ, 525, 886

Asplund, M., Grevesse, N., Sauval, A. J., & Scott, P. 2009, ARA&A, 47, 481
Beers, T. C., & Christlieb, N. 2005, ARA&A, 43, 531
Burbidge, E. M., Burbidge, G. R., Fowler, W. A., & Hoyle, F. 1957, RvMP, 29, 547
Cameron, A. G. W. 1957, PASP, 69, 201
Castelli, F., & Kurucz, R. L. 2004, arXiv:astro-ph/0405087
Cowperthwaite, P. S., Berger, E., Villar, V. A., et al. 2017, ApJL, 848, L17
Drout, M. R., Piro, A. L., Shappee, B. J., et al. 2017, Sci, 358, 1570
Frebel, A. 2018, ARA&A, submitted
Frebel, A., Casey, A. R., Jacobson, H. R., & Yu, Q. 2013, ApJ, 769, 57
Hansen, C. J., Primas, F., Hartman, H., et al. 2012, A&A, 545, A31
Hansen, T. T., Holmbeck, E. M., Beers, T. C., et al. 2018, ApJ, 858, 92
Hansen, T. T., Simon, J. D., Marshall, J. L., et al. 2017, ApJ, 838, 44
Henden, A. A., Templeton, M., Terrell, D., et al. 2016, VizieR Online Data Catalog, 2336, 1
Hill, V., Christlieb, N., Beers, T. C., et al. 2017, A&A, 607, A91
Hill, V., Plez, B., Cayrel, R., et al. 2002, A&A, 387, 560
Hunter, J. D. 2007, CSE, 9, 90
Ji, A. P., & Frebel, A. 2018, ApJ, 856, 138
Ji, A. P., Frebel, A., Simon, J. D., & Chiti, A. 2016, ApJ, 830, 93
Kilpatrick, C. D., Foley, R. J., Kasen, D., et al. 2017, Sci, 358, 1583
Lee, Y. S., Beers, T. C., Masseron, T., et al. 2013, AJ, 146, 132
Lee, Y. S., Beers, T. C., Sivarani, T., et al. 2008a, AJ, 136, 2022
Lee, Y. S., Beers, T. C., Sivarani, T., et al. 2008b, AJ, 136, 2050
Liu, C., Deng, L.-C., Carlin, J. L., et al. 2014, ApJ, 790, 110
Mashonkina, L., Christlieb, N., & Eriksson, K. 2014, A&A, 569, A43
Meyer, B. S. 1994, ARA&A, 32, 153
Nishimura, N., Sawai, H., Takiwaki, T., Yamada, S., & Thielemann, F.-K. 2017, ApJL, 836, L21
Placco, V. M., Frebel, A., Beers, T. C., & Stancliffe, R. J. 2014, ApJ, 797, 21
Placco, V. M., Holmbeck, E. M., Frebel, A., et al. 2017, ApJ, 844, 18
Roederer, I. U., Mateo, M., Bailey, J. I., III, et al. 2016, AJ, 151, 82
Roederer, I. U., Preston, G. W., Thompson, I. B., et al. 2014, AJ, 147, 136
Sakari, C. M., Placco, V. M., Hansen, T., et al. 2018, ApJL, 854, L20
Schatz, H., Toenjes, R., Pfeiffer, B., et al. 2002, ApJ, 579, 626
Schlafly, E. F., & Finkbeiner, D. P. 2011, ApJ, 737, 103
Shappee, B. J., Simon, J. D., Drout, M. R., et al. 2017, Sci, 358, 1574
Siqueira Mello, C., Hill, V., Barbuy, B., et al. 2014, A&A, 565, A93
Skrutskie, M. F., Cutri, R. M., Stiening, R., et al. 2006, AJ, 131, 1163
Sneden, C. 1973, ApJ, 184, 839
Sneden, C. 2002, in IAU Symp. 187, Cosmic Chemical Evolution, ed. K. Nomoto & J. W. Truran (Dordrecht: Kluwer), 81
Sneden, C., Cowan, J. J., & Gallino, R. 2008, ARA&A, 46, 241
Sobeck, J. S., Kraft, R. P., Sneden, C., et al. 2011, AJ, 141, 175
Tody, D. 1993, in ASP Conf. Ser. 52, Astronomical Data Analysis Software and Systems II, ed. R. J. Hanisch, R. J. V. Brissenden, & J. Barnes (San Francisco, CA: ASP), 173
Tull, R. G., MacQueen, P. J., Sneden, C., & Lambert, D. L. 1995, PASP, 107, 251
Wanajo, S., & Ishimaru, Y. 2006, NuPhA, 777, 676